

AN EXPERIMENTAL AND NUMERICAL STUDY OF THE HYDROELASTIC BEHAVIOR OF AN HYDROFOIL IN TRANSIENT PITCHING MOTION

Antoine Ducoin^{1,*}, Jacques André Astolfi¹, François Deniset¹, Jean-François Sigrist²

¹ Institut de Recherche de l'Ecole Navale EA 3634, Ecole Navale, 29240 Brest Armées, France

² DCNS Propulsion, 44620, La Montagne, France
antoine.ducoin@ecole-navale.fr

ABSTRACT

The structural behavior of a deformable hydrofoil in forced pitching motion is analyzed through an experimental and a numerical approach. The experimental study is based on the measurement of the wall pressure on a rigid hydrofoil and the tip section displacement of an equivalent deformable hydrofoil. The numerical computations are carried out through a weak coupling between a CFD finite volume code and a CSD finite element code. The structural response appears to be strongly linked to hydrodynamic phenomena such as boundary layer laminar to turbulent transition and leading edge vortex shedding. The influence of pitching velocity is discussed. Finally, the paper presents preliminary results on Cavitation Structure Interaction (CSI).

INTRODUCTION

The knowledge of the hydrodynamic loading and deformation on lifting bodies operating in transient regimes is very important for marine structure design and sizing of rudders, stabilizers or marine propellers. Many efforts were made in the past decades in order to approach through simulations the real loading for which some complex hydrodynamic and fluid structure interaction phenomena occur (Young (2008)). The possibility to take into account those phenomena comes from the recent development of numerical methods and models which allow to compute complex flows with reasonable CPU time (Menter et al. (2006)). The unsteady nature of the flow in the case of transient regimes can have impact on load predictions (Triantafyllou et al. (1993)). The knowledge of the pressure field distribution on the body and its evolution in time can then bring new elements in the understanding of the phenomena of dynamic loading induced by high pitching velocities (Jumper et al. (1987), Hamdani and Sun (2000)). An experimental study is presented in Lee and Gerontakos (2004) for an oscillating airfoil at various pitching velocities and at $Re = 1.35 \times 10^5$. For small values of pitching velocity,

boundary layer events produce variations in lift, drag and moment coefficients. As well, it has influence on boundary layer transition caused by laminar separation which is delayed and promoted when pitching velocity increases.

As far as aerodynamic applications are concerned, many studies have highlighted that structural deformation of an elastic solid under static or dynamic loads may be of primary importance in the evaluation of aerodynamic performances (Bhardwaj (1997), Send (1999), Lund et al. (2003), Engel and Griebel (2006), Patil and Hodges (2004)).

In the context of hydroelasticity, Young (2007) and Young (2008) presented an approach applied to a cavitating propeller which takes into account the modification of fluid pressure field induced by the blade displacement. It can be assumed that structural deformations can have a strong impact on cavitation behavior. Indeed, the structural deformation and the local incidence variation induced by twist deformation can modify the cavitation inception and development.

The paper focus on an experimental and numerical study of the hydroelastic behavior of an hydrofoil in transient pitching motion. First, the experimental set up and the computation methods are presented. Then, the results of the wall pressure measurement on a rigid hydrofoil are exposed. The experimental and computed tip section displacements of a deformable hydrofoil are then presented. Finally, the influence of pitching motion and hydrofoil deformation on cavitation development is examined.

1 EXPERIMENTAL SET UP

Measurements are carried out in the cavitation tunnel at IRENav. The test section is 1 m long and has a 0.192m square section. The velocity ranges between 0 and 15m/s and the pressure range from 30 mbar to 3 bars. The hydrofoil is a NACA 66 with a camber ratio of 2% and a relative thickness of 12% (Leroux et al. (2005)). The chord is $c=0.148$ m and the span is $b=0.191$ m.

Two experimental set up are used in this paper. First, we consider the wall pressure analysis on a rigid hydro-

foil in stainless steel which is mounted horizontally in the tunnel test section. Pressure measurements are carried out using piezo-resistive transducers of 10 bars maximum pressure. The pressure transducers are mounted into small cavities with a 0.5 mm diameter pinhole at the hydrofoil surface. Experiments are led with a sample frequency of $f = 20\text{ kHz}$. An analysis of suction side loading was done by summing pressure coefficients on the suction side. The approximation can be written as:

$$C_l(t) = \sum_{i=2}^{10} C_p(x_i/c, t) \Delta(x_i/c) \quad (1)$$

where $C_p(\frac{x_i}{c}, t)$ is the pressure coefficient at location $\frac{x_i}{c}$ and $\Delta(\frac{x_i}{c})$ is the non dimensional distance between two consecutive transducers. The procedure is applied to numerical data for comparison.

The nominal free stream velocity V_∞ is 5 m/s , corresponding to a Reynolds number based on the foil chord length of $Re = 0.75 \times 10^6$. The hydrofoil rotates about an axis located at $x/c = 0.25$. The angle of incidence varies from 0° to 15° and then comes back to 0° , with at least 2 periods of acceleration and 2 periods of deceleration. As shown in figure 1, four pitching velocities are defined, from a slow pitching velocity to a high one. The average rotation velocity is $\dot{\alpha} = 2\alpha_{max}/t_f$, where t_f the total time of transient motion. A reduced pitching velocity is introduced $\dot{\alpha}^* = \frac{\dot{\alpha} \times c}{V_\infty}$ (Figure 1). Upward angles of incidences are noted α_1 and downward angles of incidences are noted α_2 .

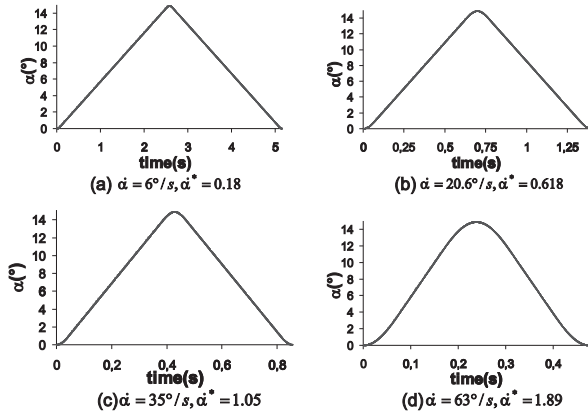


Figure 1. Pitching velocities, angle of incidence versus time, $V_\infty = 5\text{ m/s}$

For fluid-structure coupling analysis, we consider a deformable hydrofoil with a plastic material (POM Polyacetate, $E=3000\text{ MPa}$). The hydrofoil root section is clamped and the tip section is free (Figure 2). Experiments are performed with a visual system to estimate the tip section displacement. A video camera is used in order to get a side

view of the hydrofoil and then measure the dynamic free tip section displacement by image processing. A set of pictures is recorded at a frequency of 100 Hz which allow us to measure the structure displacement during the pitching motion. The image processing uncertainties correspond to the precision of the method used to capture the foil position. It is about 2 pixels, which leads to an uncertainty of about $\Delta = 0.14\text{ mm}$ on the hydrofoil displacements.

In the last section, the pressure into the tunnel test section is decreased in order to obtain cavitation for the same free stream velocities and the same pitching velocities. It is based on the cavitation number defined as $\sigma = \frac{P_0 - P_V}{1/2\rho U_\infty^2}$ where P_0 is the pressure in the tunnel test section and P_V is the vapor pressure.

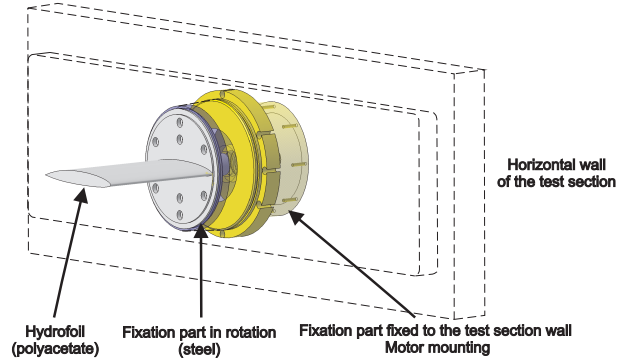


Figure 2. Deformable hydrofoil set up

2 COMPUTATIONAL METHOD

The fluid structure problem is solved with the finite volume technique using the CFD code *CFX*® for the fluid, and the finite element code using the CSD code *ANSYS*® for the structure. In this section, the fluid structure equations are given and the numerical discretization and resolution is described.

2.1 Governing equation for the fluid and the structure

One one hand, the fluid flow is described with the mass and momentum conservation equations which read for an incompressible and viscous fluid:

$$\frac{\partial v_j}{\partial x_j} = 0 \quad (2)$$

$$\frac{\partial(\rho_F v_i)}{\partial t} + \frac{\partial(\rho_F v_i v_j)}{\partial x_j} = -\frac{\partial p}{\partial x_i} + \mu \frac{\partial^2 v_i}{\partial x_j^2} \quad (3)$$

On the other hand, the structure behavior is described in the frame of linear elasticity, using a displacement formulation:

$$\rho_S \frac{\partial^2 u_i}{\partial t^2} - \frac{\partial \sigma_{ij}(\mathbf{u})}{\partial x_j} = 0 \quad (4)$$

The structure is subjected to imposed local fluid forces which are derived from the fluid stress tensor; boundary condition of the structure problem on the fluid structure interface reads:

$$\sigma_{ij}(\mathbf{u}) \cdot n_j = \left[-p\delta_{ij} + \mu \left(\frac{\partial v_i}{\partial x_j} + \frac{\partial v_j}{\partial x_i} \right) \right] \cdot n_j \quad (5)$$

A more complete resolution at the fluid structure interface is to take into account the structure displacement and then add a boundary condition for the fluid. It is not considered in this study for computer time cost reason, but this will be taken into account in future works.

2.2 Discretization and resolution of the fluid structure domain

A coupled "one way" computation is shown in Figure 3. At each physical time step, the flow is resolved, then the pressure field is exported from the CFD code to the CSD code at the fluid structure interface using an interpolation procedure. When a new time step begins, the fluid domain is remeshed resulting from the rotation imposed on the fluid and a new computation is performed.

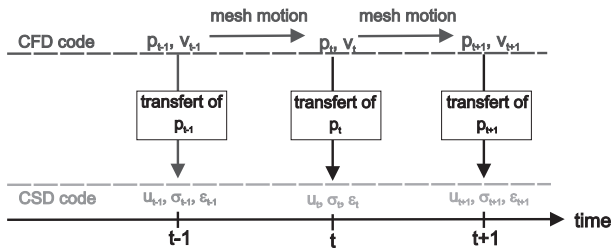


Figure 3. One way coupling between a CDS and a CFD code

The fluid calculations are carried out with the CFD RANS based code CFX. This is a finite volumes code where equations 2 and 3 are integrated over a control volume, using the Leibnitz rule and the Gauss theorem. Concerning the hydrodynamics models, the $k - \omega SST$ is used because it appears to be an accurate turbulence model for boundary layer detachment prediction (Menter (1993), Menter et al. (2003), Haase et al. (2006)).

The $k - \omega SST$ turbulence model is coupled with a transition model $\gamma - Re_\theta$ which uses experimental correlations based on local variables (Abu-Ghannam and Shaw (1980), Steelant and Dick (1996), Menter et al. (2006)). A previous study Ducoin et al. (2008) have highlighted the importance to take into account the transition in the hydrodynamic loading prediction in the present case. This transition model use local variables to activate the production term in the intermittency equation. It allows us to capture major transition effects in the case of separation induced transition. The intermittency is modified to accept values larger than 1 at separation in order to have a correct prediction of transition length. Complete transition model formulation is given in Menter et al. (2006).

The 3D domain correspond to the tunnel test section at IRENav. The inlet velocity is set to $V_\infty = 5m/s$ and the taken outlet reference pressure is set to zero. Symmetry conditions are set on horizontal walls and a no slip condition is imposed on the hydrofoil surface. Transient computations are initialized with a stationary converged computation.

As shown in figure 4, the mesh is composed of 3 500 000 elements and 30 layers are used in the structured near wall zone. The other part of the domain is discretized with unstructured triangle elements. The boundary layer is discretized in order to satisfy $y^+ \approx \frac{y u_\tau}{\nu} = 1$. This ensures a low Reynolds resolution. Mesh refinements are performed at the leading edge, at the trailing edge and in the wake. The 3D mesh has been done in order to reproduce the events like laminar separation bubble, transition and massive stall prediction which has been investigated in a 2D study in witch we consider a rigid hydrofoil (Ducoin et al. (2008)). The hydrofoil motion is taken into account using a changing boundary condition at the wall. To do that, foil mesh coordinates are calculated at each time step and the whole domain is then meshed again. This technique uses a diffusivity parameter applied in the mesh displacement equation which induces a mesh stiffness (Maman and Farhat (1995)). This one is set to be inversely proportional to the wall distance in order to limit mesh distortion in the wall region. The RANS equations are solved in an arbitrary referential with the Arbitrary Lagrangian Euler formulation (ALE) Farhat et al. (1998).

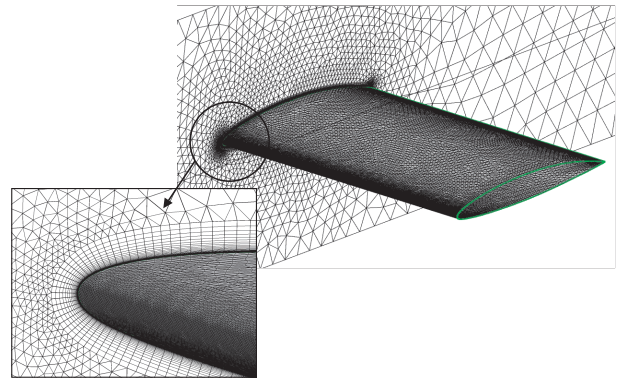


Figure 4. 3d mesh of the fluid domain

The structure is solved with the CSD finite element code ANSYS. The hydrofoil is discretized with three-dimensional ten-node tetrahedral elements of quadratic behavior. The fixation system of the foil is rigid. For this reason, it is not considered in the calculation and a clamped condition is set on the root section, whereas the tip section is free. The structure computation is assumed to be dynamic at each time step and the pressure field computed from the CFD transient simulation is interpolated at the fluid structure interface.

3 RESULTS AND DISCUSSION

The Figure 5 show the suction side loading for the four pitching velocities. The impact of laminar to turbulent transition is clearly shown. It induce a significant slope modification at $\alpha^+ = 5^\circ$ for the slower pitching velocity. The transition is caused by a laminar separation bubble at the leading edge, Ducoin et al. (2008). As shown, increasing pitching velocities have an impact on boundary layer transition. It is observed that the transition is delayed. This results in an increase of the hydrofoil loading and a much higher value at stall. Overshoots are observed during stall resulting from leading edge vortex shedding, at approximately $f = 6Hz$. During the downward motion to $\alpha_2 = 0^\circ$, a strong hysteresis effect is observed for the highest pitching velocity.

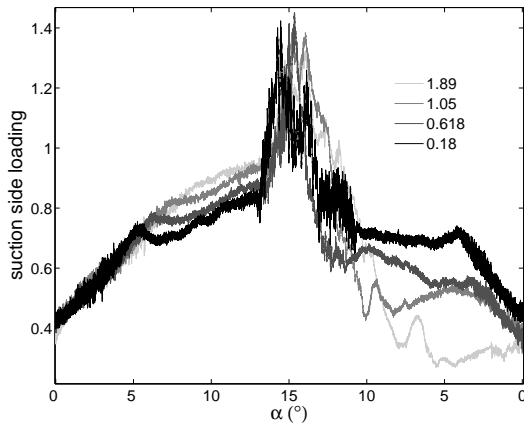


Figure 5. Experimental suction side loading for 4 pitching velocities, Eq.1

The tip section displacement was measured on a deformable hydrofoil. An exemple of tip section displacement is show in Figure 6 for $V_\infty = 7m/s$ at $\alpha = 15^\circ$. The dashed line is the non-deformed tip section ($V_\infty = 0m/s$). As shown, the displacement increase with an increase of the pitching velocity, see Figure 6 (a) $\dot{\alpha}^* = 0.12$ and Figure 6 (b) $\dot{\alpha}^* = 1.35$. The maximum displacement has been measured for the static case and for the four pitching velocities at $V_\infty = 5m/s$ (Figure 7). The comparison of Figure 5 and 7 shows that the tip section displacement is directly linked to the hydrodynamic loading. Five steps can be noticed during the pitching motion (Figure7):

1. From $\alpha^+ = 0^\circ$ to 5° : displacements increase linearly as well as the hydrodynamic loading whatever the pitching velocity.
2. At $\alpha^+ \approx 5^\circ$: differences can be seen. For the lowest pitching velocity and the static measurements, an inflection of the displacement is observed. It is delayed and reduced when pitching velocity increase. It is almost suppressed for the highest pitching velocity. It agrees with the pressure inflection due to transition shown in Figure 5. As a consequence, the structure

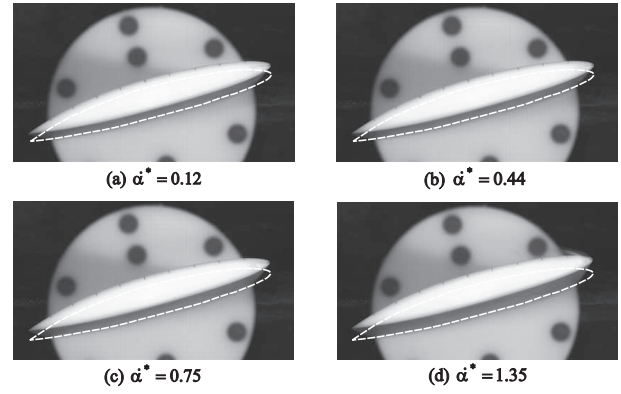


Figure 6. tip section measurement for 4 pitching velocities at $\alpha = 15^\circ$, $V_\infty = 7m/s$

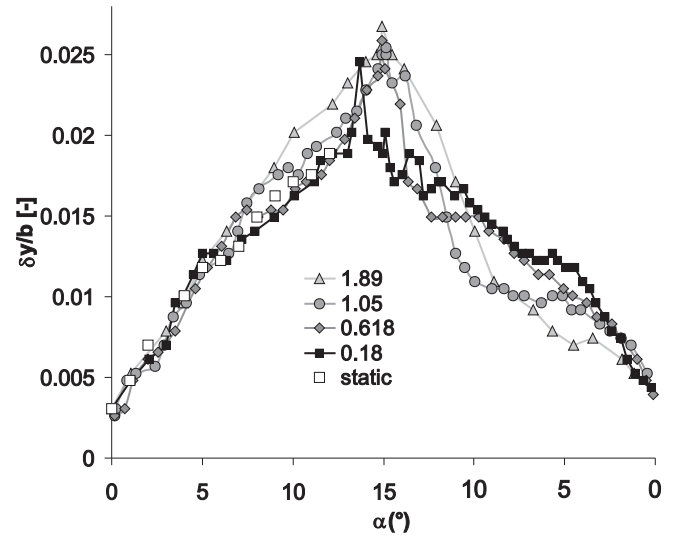


Figure 7. maximum displacement for 4 pitching velocities, $V_\infty = 5m/s$

behavior is affected by the transition from laminar to turbulent.

3. From $\alpha^+ \approx 5^\circ$ to 13° : the displacement level increases with pitching velocity. Around 13° , the maximum displacement is about $\delta_y = 0.018$ for $\dot{\alpha}^* = 0.18$ and $\delta_y = 0.024$ for $\dot{\alpha}^* = 1.89$.
4. From $\alpha^+ \approx 13^\circ$ to $\alpha^- \approx 13^\circ$ (return step): displacement fluctuation are observed. Three peaks are observed for $\dot{\alpha}^* = 0.18$: a high amplitude peaks at $\alpha^+ = 14.5^\circ$ followed by two lower peaks at respectively $\alpha^- = 14.5^\circ$ and $\alpha^- = 13^\circ$. Again it agrees with the pressure measurements showing high amplitude pressure fluctuations resulting from stall and leading edge vortex shedding.
5. From $\alpha^- \approx 13^\circ$ to 0° : an hysteresis is observed when pitching velocity increases. As an exemple, at $\alpha^+ = \alpha^- = 5^\circ$, the displacement are both $\delta_y = 0.0183$ for $\dot{\alpha}^* = 0.18$ whereas displacements are respectively $\delta_y = 0.0183$ and $\delta_y = 0.0068$ for $\dot{\alpha}^* = 1.89$.

One way computations are performed through the

method described in Figure 3. Experimental results for maximum displacement of the tip section are given in Figures 8 and 9 and compared to the computational results obtained by the one way computations. For the two pitching velocities considered, results are in good agreement. The difference is weak for small angle of incidence, and tend to increase after the transition, starting at $\alpha = 5^\circ$ for $\dot{\alpha}^* = 0.18$ and $\alpha = 9^\circ$ for $\dot{\alpha}^* = 1.89$. The displacement fluctuations due to stall are observed by computations. Leading edge vortex shedding appears to have the same influence for the lowest pitching velocity $\dot{\alpha}^* = 0.18$ whereas a stronger hysteresis effect is observed in computation for the highest pitching velocity $\dot{\alpha}^* = 1.89$. The difference between experiments and computations can be attributed to damping which is not taken into account in the structure model.

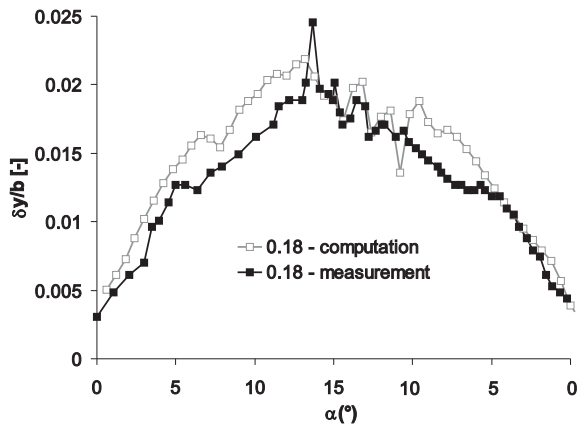


Figure 8. Computation versus measurement for maximum displacement during pitching motion, $\dot{\alpha}^* = 0.18$

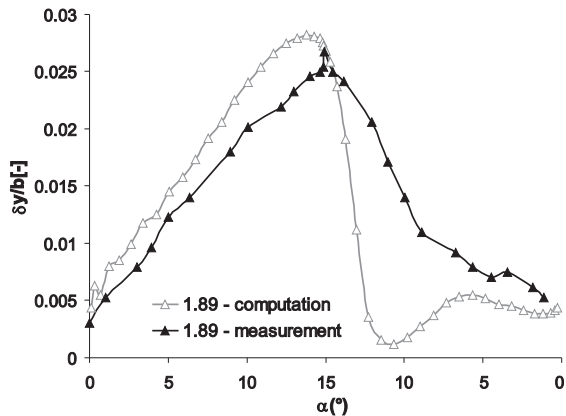


Figure 9. Computation versus measurement for maximum displacement during pitching motion, $\dot{\alpha}^* = 1.89$

An investigation of Cavitation Structure Interaction (CSI) was carried out experimentally for $\dot{\alpha}^* = 0.18$ and $\dot{\alpha}^* = 1.89$. Displacements are measured with the same

method than for non cavitating flow and another video camera is used in order to observed cavitation.

The cavitation is obtained by decreasing the pressure in the tunnel test section in order to obtained the cavitation inception at a static angle of incidence of $\alpha = 8^\circ$, this corresponds to a cavitation number $\sigma = 3$. The cavitation pattern is characterized by a band at the leading edge (Figure 10). Then, the cavitation inception is observed for transient



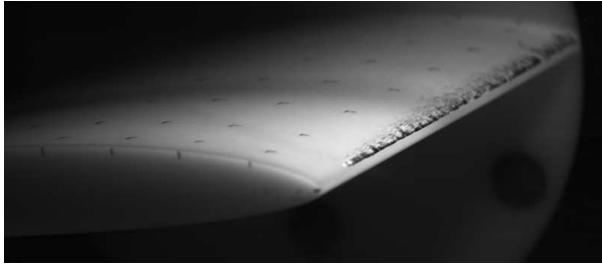
Figure 10. Cavitation inception at the leading edge for a fixed angle of incidence, $\alpha = 8^\circ$, $\sigma = 3$

pitching motions. For the lower pitching velocity, the cavitation inception is the same as in the static case but it is delayed of about 1° (Figure 11 (a)). For the highest pitching velocity $\dot{\alpha}^* = 1.89$ (Figure 11 (b)), the cavitation inception is delayed up to $\alpha = 11^\circ$ and appear as an attached cavity at the leading edge. The delay and modification of cavitation pattern is due to the delay of laminar to turbulent transition at the leading edge when pitching velocity increases. Whereas Reynolds number and pressure in the test section are the same, differences exist in the cavitation patterns for the two pitching velocities. The lowest pitching velocity is characterized by intermediate cavities. The length increases up to $0.15c$ and has a relatively stable behavior. Shedding of small vapor structures is observed at high angle of incidences which has a few influence on structure deformation. The highest pitching velocity shows a relatively long sheet cavity which develop from the leading edge up to $0.4c$. Moreover, 3D effects appear through the span.

Figure 12 shows the cavitation pattern obtained for the maximum angle of incidence $\alpha = 15^\circ$. For the lowest pitching velocity, the cavitation is induced by vortex shedding at the leading edge (Figure 12 (c)). It is characterized by transversal streaks along the span. In that case, the impact on structural displacement is close to the sub-cavitation case as shown in Figure 12 (a). The highest

pitching velocity exhibits an instable sheet cavity inducing a large shedding of vapor-filled structure (Figures 12 (d)). In that case the cavitation has a strong impact on the structure behavior. Indeed, the tip section with cavitation shows higher displacement than the tip section without cavitation, Figure 12 (b).

The impact of cavitation on displacement during the pitching motion is shown in Figure 13 for $\dot{\alpha}^* = 0.18$ by compar-



(a) $\dot{\alpha}^* = 0.18$, $\alpha = 9.5^\circ$, perspective view



(b) $\dot{\alpha}^* = 1.89$, $\alpha = 11^\circ$, perspective view

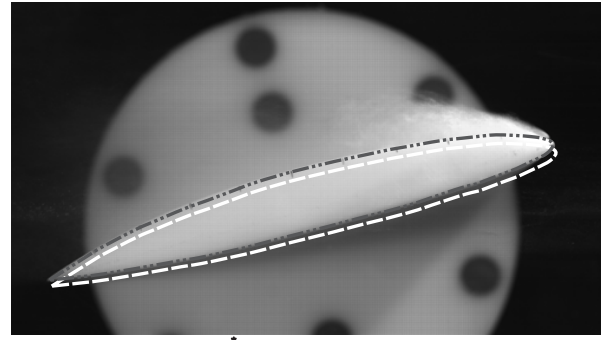
Figure 11. Effects of pitching velocity on cavitation inception at the leading edge, $V_\infty = 5m/s$ and $\sigma = 3$. Dotted white line is the non deformed section

ing maximum displacements for cavitating and non cavitating flows. The range of angle of incidence where cavitation appears are shown by a dashed square. Displacements are quite the same at the beginning of the motion up to the cavitation inception, except from 6 to 8° where a difference can be seen after transition. Intermediate cavities increase displacement between $10^\circ \leq \alpha^+ \leq 13^\circ$. This effect disappears when vortex shedding occurs, then displacements with and without cavitation show fluctuations of the same order of magnitude. When the flow reattaches, a slight difference is observed. When cavitation disappears, the same evolution is observed to the backward motion.

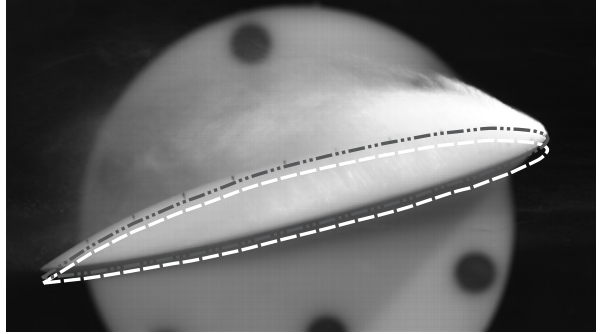
The displacement analysis for $\dot{\alpha}^* = 1.89$ in Figure 14 shows that the unstable behavior of the sheet cavity has more influence on the structure. Displacements are higher than the case $\dot{\alpha}^* = 0.18$ and the cavity inception at the leading edge induces a global increase of displacements. When the cavity develops, displacement stop to increase until the cavity collapse. A peak is then visible on Figure 14 at $\alpha = 15^\circ$, followed by a stronger hysteresis effect $0^\circ \leq \alpha_- \leq 6^\circ$.

CONCLUSION

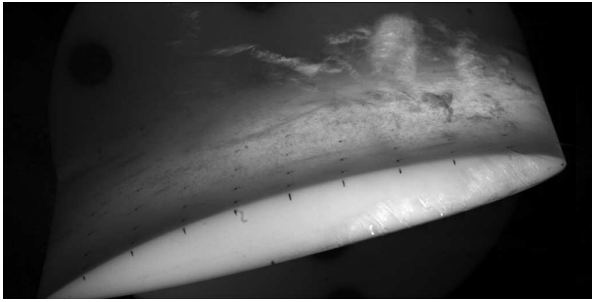
Experiments and computations on a deformable hydrofoil in a transient pitching motion have been carried out. It was shown that the structure responds linearly to the transient hydrodynamic loading. The hydrofoil displacements are affected by the laminar to turbulent transition for small values of pitching velocity whereas the highest pitching velocity suppresses the effect. Fluctuating displacements have been observed when leading edge vortex shedding occurs during stall, for both numerical and experimental approaches. It is followed by a strong hysteresis when the



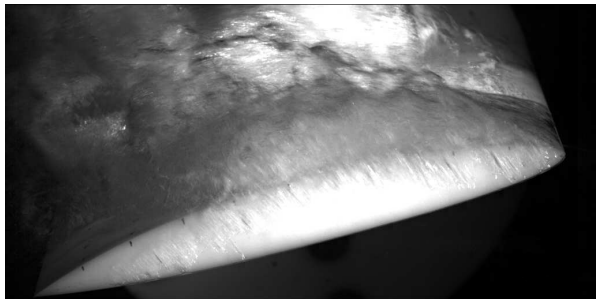
(a) $\dot{\alpha}^* = 0.18$, $\alpha = 15^\circ$, side view



(b) $\dot{\alpha}^* = 1.89$, $\alpha = 15^\circ$, side view



(c) $\dot{\alpha}^* = 0.18$, $\alpha = 15^\circ$, perspective view



(d) $\dot{\alpha}^* = 1.89$, $\alpha = 15^\circ$, perspective view

Figure 12. Effects of pitching velocity on cavitation development, $\alpha = 15^\circ$, $\sigma = 3$, $Re = 750\,000$, $V_\infty = 5m/s$, white dashed line: non deformed tip section, black dashed line: non-cavitating deformed tip section

hydrofoil returns to its initial angle of incidence 0° . Similar measurements have been carried out in the case of cavitating flows for the lowest and the highest pitching velocity. Displacements have been measured and the cavitation behavior is observed at the same time. Different types of cavitation were observed. For the lowest pitching velocity, it is characterized by intermediate cavities with a relatively stable behavior and shedding of small vapor structures are observed at higher angles of incidence. In that

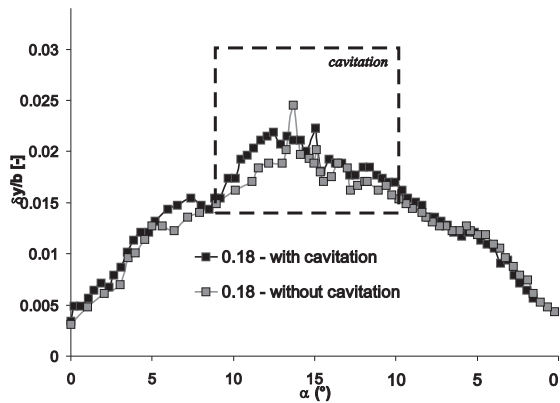


Figure 13. Effect of cavitation on maximum displacement, $\dot{\alpha}^* = 0.18$, $Re = 750\,000$, $V_\infty = 5\text{ m/s}$

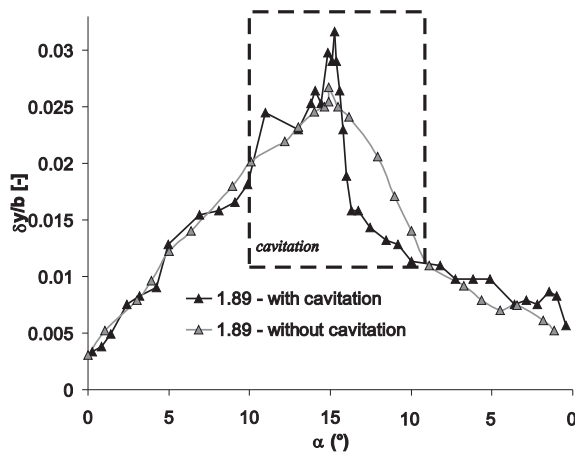


Figure 14. Effect of cavitation on maximum displacement, $\dot{\alpha}^* = 1.89$, $Re = 750\,000$, $V_\infty = 5\text{ m/s}$

case, the impact on the structure displacement is weak. For the highest pitching velocity shows a relatively long sheet cavity which develops from the leading edge up to $0.4c$. The cavity has a unstable behavior and has a strong impact on structure displacements. Moreover, the structure displacement probably has an impact on cavitating behavior too. This point is under investigation under investigation through experimental and numerical approaches.

ACKNOWLEDGMENT

The authors gratefully acknowledge the technical staff of IRENav for its contribution to the experimental set up.

REFERENCES

Abu-Ghannam, B. J., Shaw, R., 1980. Natural transition of boundary layers-The effects of turbulence, pressure gradient, and flow history. *Journal of Mechanical Engineering Science* 22, 213–228.

Bhardwaj, M. K., 1997. A CFD/CSD interaction methodol-

ogy for aircraft wings. Ph.D. thesis, Virginia Polytechnic Institute and State University.

Ducoin, A., Astolfi, J. A., Deniset, F., Sigrist, J. F., 2008. An experimental and numerical investigation of flow over a hydrofoil in transient regimes based on wall-pressure analysis. In: *ASME Pressure Vessels and Piping conference*, Chicago.

Engel, M., Griebel, M., 2006. Flow simulation on moving boundary-fitted grids and application to uid-structure interaction problems. *Int. J. Numer. Meth. Fluids* 50, 437–468.

Farhat, C., Lesoinne, M., Le Tallec, P., 1998. Load and motion transfer algorithms for fluid/structure interaction problems with non-matching discrete interfaces: Momentum and energy conservation, optimal discretization and application to aeroelasticity. *Computer Methods in Applied Mechanics and Engineering* 157 (1-2), 95–114.

Haase, W., Aupoix, B., Bunge, U., Schwamborn, D., 2006. *FLOMANIA-A European Initiative on Flow Physics Modelling*. Berlin: Springer, 2006. ISBN 3-540-28786-8.

Hamdani, H., Sun, M., 2000. Aerodynamic forces and flow structures of an airfoil in some unsteady motions at small Reynolds number. *Acta Mechanica* 145 (1), 173–187.

Jumper, E., Schreck, S., Dimnick, R., 1987. Lift-curve characteristics for an airfoil pitching at constant rate. *Journal of aircraft* 24 (10), 680–687.

Lee, T., Gerontakos, P., 2004. Investigation of flow over an oscillating airfoil. *Journal of Fluid Mechanics* 512, 313–341.

Leroux, J. B., Coutier-Delgosha, O., Astolfi, J. A., 2005. A joint experimental and numerical study of mechanisms associated to instability of partial cavitation on two-dimensional hydrofoil. *Physics of Fluids* 17, 052101.

Lund, E., Møller, H., Jakobsen, L. A., 2003. Shape design optimization of stationary fluid-structure interaction problems with large displacements and turbulence. *Structural and Multidisciplinary Optimization* 25 (5), 383–392.

Maman, N., Farhat, C., 1995. Matching fluid and structure meshes for aeroelastic computations: A parallel approach. *Computers and Structures* 54 (4), 779–785.

Menter, F. R., 1993. Improved Two-Equation k-Turbulence Models for Aerodynamic Flows. *NASA Technical Memorandum* 103975, 34.

Menter, F. R., Kuntz, M., Langtry, R., 2003. Ten Years of Industrial Experience with the SST Turbulence Model. *Turbulence, Heat and Mass Transfer* 4, 625–632.

Menter, F. R., Langtry, R., Völker, S., 2006. Transition Modelling for General Purpose CFD Codes. *Flow, Turbulence and Combustion* 77 (1), 277–303.

Patil, M. J., Hodges, D. H., 2004. On the importance of aerodynamic and structural geometrical nonlinearities in aeroelastic behavior of high-aspect-ratio wings. *Journal of Fluids and Structures* 19 (7), 905–915.

Send, W., 1999. Coupling of Fluid and Structure for Transport Aircraft Wings. In: *International Forum on Aeroelasticity and Structural Dynamics*, CEAS/AIAA/ICASE/NASA, Langley, Williamsburg,

VA, June.

- Steelant, J., Dick, E., 1996. Modelling of bypass transition with conditioned intermittency transport equation. *International journal for numerical methods in fluids* 23, 193–220.
- Triantafyllou, G. S., Triantafyllou, M. S., Grosenbaugh, M., 1993. Optimal thrust development in oscillating foils with application to fish propulsion. *Journal of Fluids and Structures* 7 (2), 205–224.
- Young, Y. L., 2007. Time-dependent hydroelastic analysis of cavitating propulsors. *Journal of Fluids and Structures* 23 (2), 269–295.
- Young, Y. L., 2008. Fluid–structure interaction analysis of flexible composite marine propellers. *Journal of Fluids and Structures*.